西安交通大学
XI'AN JIAOTONG UNIVERSITY

World Scientific
www.worldscientific.com

Enhanced magneto-dielectric response in La-doped Co2U hexaferrite

Parambir Singh Malhi[*], Anupinder Singh[†], Mandeep Singh[†], Sachin Kumar[*],
Shubhpreet Kaur[†], Mehak Arora[†] and Ashwani Kumar Sood[*,‡]

[*]*Department of Chemistry, UGC Centre for Advanced Studies II, Faculty of Sciences*
Guru Nanak Dev University, Amritsar 143005, Punjab, India

[†]*Multifunctional Materials Laboratory, Department of Physics, Faculty of Sciences*
Guru Nanak Dev University, Amritsar 143005, Punjab, India

[‡]aksoodchem@yahoo.co.in

The U-type hexaferrites $(Ba_{1-3x}La_{2x})_4Co_2Fe_{36}O_{60}$ ($x = 0$, 0.05, 0.10, 0.15, 0.20, 0.25) have been synthesized by auto-combustion method. The work involves the study of structural, microstructural, dielectric, magnetic and magneto-dielectric properties of the prepared materials. The structural analysis has been done by X-ray diffraction technique along with Le Bail refinement which confirmed the pure hexagonal phase for all the samples. The microstructural analysis has been carried out by field-emission scanning electron microscopy. The vibrating sample magnetometer is used to measure the magnetic properties. The sample with a composition of $x = 0.15$ has shown the maximum magnetization of approximately 73.31 emu/g with the remnant magnetization of 38.89 emu/g and coercive field of 1.77 kOe at room temperature. Moreover, the same sample has delivered the maximum magneto-dielectric response of about 54.18% at 1.5-T field.

Keywords: U-type hexaferrites; magneto-dielectric properties.

1. Introduction

Hexaferrites are complex ferrites having a magneto-plumbite structure. The stable hexaferrites show complexity in the ascending order as M-, Y-, W-, Z-, X- and U-type hexaferrites.[1,2] Among these, U-type hexaferrites have the highest saturation magnetization (M_s) and substantial intrinsic magneto-crystalline anisotropy (MCA).[2–16] Moreover, a U-type hexaferrite with the chemical formula of $Ba_4Co_2Fe_{36}O_{60}$ (Co2U) has a comparatively complicated structure, the largest unit cell and the highest magnetic properties.[3,17] Lisjak *et al*. have outlined the optimized synthesis conditions for Co2U hexaferrite,[13] and suggested the $R3m$ crystal symmetry with a stacking sequence of SRS*R*S*T bricks, where the * symbol designates the 180° spinning of the brick about the *c*-axis.[2,3,10,12,13] However, Chen *et al*.,[18] Honda *et al*.[19] and Okumura *et al*.[20] recommended $R3m$ structure with a 3×(S*R*STSR) stacking sequence. In 2001, Pullar and Bhattacharya demonstrated the structural and magnetic behaviors and reported that Co2U has shown an M_s of 59.1 emu/g and a coercive field (H_c) of 590 Oe at 300 K.[2] According to the literature, the doping at Ba^{2+}, Co^{2+} and Fe^{3+} sites can modify the magnetic properties of Co2U hexaferrite by altering its dielectric and magnetic properties through dynamic charge balance.[3–10,12,15,16]

Hexaferrite Co2U has been extensively explored and utilized as perpetual magnets due to its very large magnetization (M_s), Curie temperature (T_c) and coercivity (H), environmental

stability and low price of fabrication. Several research groups have synthesized Co2U-based hexaferrites by using various techniques and investigated their physical properties. There are several researches present in the literature that particularly focused on substitution of divalent–tetravalent ions at the iron (Fe) site and observed the contrasting magnetic properties of Co2U.[9] Even though a myriad of investigations have been established to study, analyze and improve the magnetic properties of Co2U system, but the high-temperature electrical properties, microstructures and magneto-capacitance of doped Co2U have not been explored yet. In this backdrop, we have decided to evaluate the properties of the different La^{3+}-doped Co2U hexaferrites.

This work reports the synthesis and characterization of $(Ba_{1-3x}La_{2x})_4Co_2Fe_{36}O_{60}$, where $x = 0$, 0.05, 0.10, 0.15, 0.20 and 0.25. The structural, microstructural and magnetic properties of all the samples are investigated thoroughly. Afterwards, the electrical properties of the prepared samples are examined with the help of impedance spectroscopy. Moreover, the magneto-capacitance behavior is also analyzed and reported in this work.

2. Experimental

$(Ba_{1-3x}La_{2x})_4Co_2Fe_{36}O_{60}$, where $x = 0$, 0.05, 0.10, 0.15, 0.20 and 0.25, were synthesized via auto-combustion route.

[‡]Corresponding author.

The powders of barium nitrate [Ba(NO$_3$)$_2$], cobalt nitrate [Co(NO$_3$)$_2$·6H$_2$O], ferric nitrate [Fe(NO$_3$)$_2$·9H$_2$O] and lanthanum nitrate [La(NO$_3$)$_2$·6H$_2$O] in stoichiometric proportion were first dissolved in distilled water containing citric acid at room temperature. After continuous heating at 200°C for 6 h, a self-ignitable gel-based complex was formed in air. This gel was converted into powder after heat treatment at 600°C for 2 h followed by 12 h of heating at 1000°C in high-temperature furnace. Afterwards, PVA binder (2 wt.%) was mixed with the prepared powder for the formation of pellets. The pellets of round shape having a diameter of 10 mm and a thickness of 1 mm were formed with the help of hydraulic press. The X-ray diffraction (XRD) data of all the sintered samples are taken in the range of 25–80° at a scan speed of 2°/min with Cu-Kα anode. The investigations of surface morphology and elemental confirmation have been done by using field-emission scanning electron microscopy (FESEM) and EDAX, respectively. The density measurements for all the sintered samples have been carried out using a lab-made setup based upon Archimedes principle. The electrical and magneto-capacitance properties are studied by collecting the data from impedance analyzer (Keysight E4990A, 20 Hz–10 MHz).

3. Structural Analysis

X-ray diffractograms of all the sintered samples at room temperature are shown in Fig. 1. Every sample exhibits sharp and intense peaks which reveal the crystalline nature of all the samples. Also, there are no extra peaks present which reveals that all the samples are of single phase and there is no impurity phase. For better understanding, the Le Bail refinement with constant scale factor has been done using FullProf Suite software as shown in Figs. 2(a)–2(f). The refinement has been carried out using hexagonal phase ($R3m$ space group).
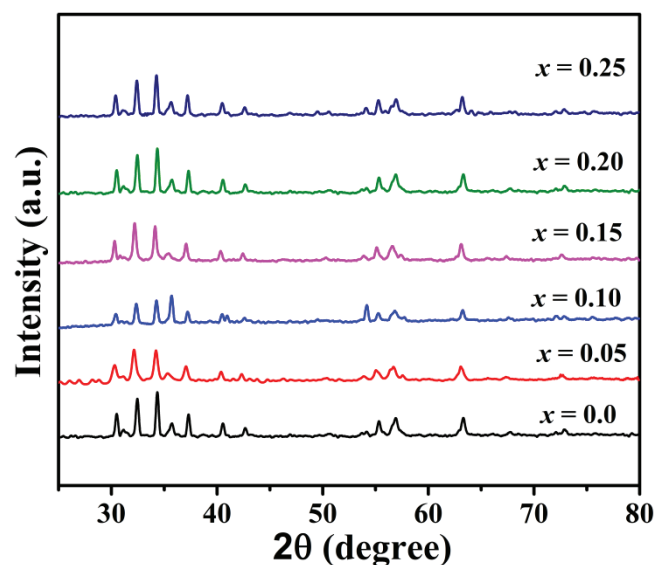

Fig. 1.   X-ray diffractograms of all the sintered samples.

The values of parameters obtained from refinement are given in Table 1. The value of goodness of fit (GOF) is less than 2 for all the samples which shows a good agreement between the observed and calculated data. The variations in the values of lattice parameters *a* and *c* are displayed in Fig. 3. It can be easily observed from the figure that the values of *a* and *c* decrease with the increase in *x* content leading to a decrease in the corresponding cell volume.

4. Morphology and Density Measurements

The surface morphology of all the samples was analyzed using FESEM. The images of the surfaces of all the samples are given in Fig. 4. All the images were recorded at a magnification of 10,000× using InLens detector. Images revealed the hexagonal structure of grains which are well defined and uniformly distributed. The grain size of all the samples was determined by using ImageJ software. The information obtained from EDAX has confirmed the elemental presence for the corresponding compositions. Moreover, the experimental values of density have been measured using Archimedes principle. The calculated grain sizes, standard deviations in grain size and density values are listed in Table 2. Clearly, a decrease in grain size is observed in all the samples which has been confirmed through density values as well as XRD data.

5. Magnetic Properties

The room-temperature magnetization versus field profiles (*M–H* loops) of all the prepared samples are shown in Fig. 5. It can be clearly seen from the figure that the saturation magnetization for all the samples is in increasing order from $x = 0$ to $x = 0.15$ and decreases afterwards. The values of saturation magnetization, coercive field and remnant magnetization for all the samples are listed in Table 3. It is evident from the table that the doping of La^{3+} ion at Ba site increases M_s from 48.19 emu/g for $x = 0$ to 73.31 emu/g for $x = 0.15$ and then decreases it to 37.22 emu/g for $x = 0.25$. The unit cell of a U-type hexaferrite exhibits the sequence of stacking blocks as SRS*R*S*T in which the large cations Ba^{2+} attain the position in oxygen lattice, whereas the Co^{2+} and Fe^{3+} cations are distributed on five different crystallographic sites; three octahedral sites, one tetrahedral site and one trigonal–bipyramidal site.[16,21] Moreover, the opposite spins are coupled together through exchange interaction via the O^{2-} ions.[16] From Table 1, it has been observed that the *c/a* ratio decreases continuously due to the smaller ionic radius of La^{3+} in comparison to Ba^{2+}. This decrease in *c/a* ratio strengthens the superexchange interaction in Fe^{3+}–O–Fe^{3+} which in turn leads to higher magnetization value.[16,21,22] Further doping causes decrement in M_s values which may be due to the magnetic dilution of Fe^{3+} into Fe^{2+} ions at octahedral sites.[16,21–24] The comparison of magnetization values for different materials from the literature is given in Table 4. This table shows
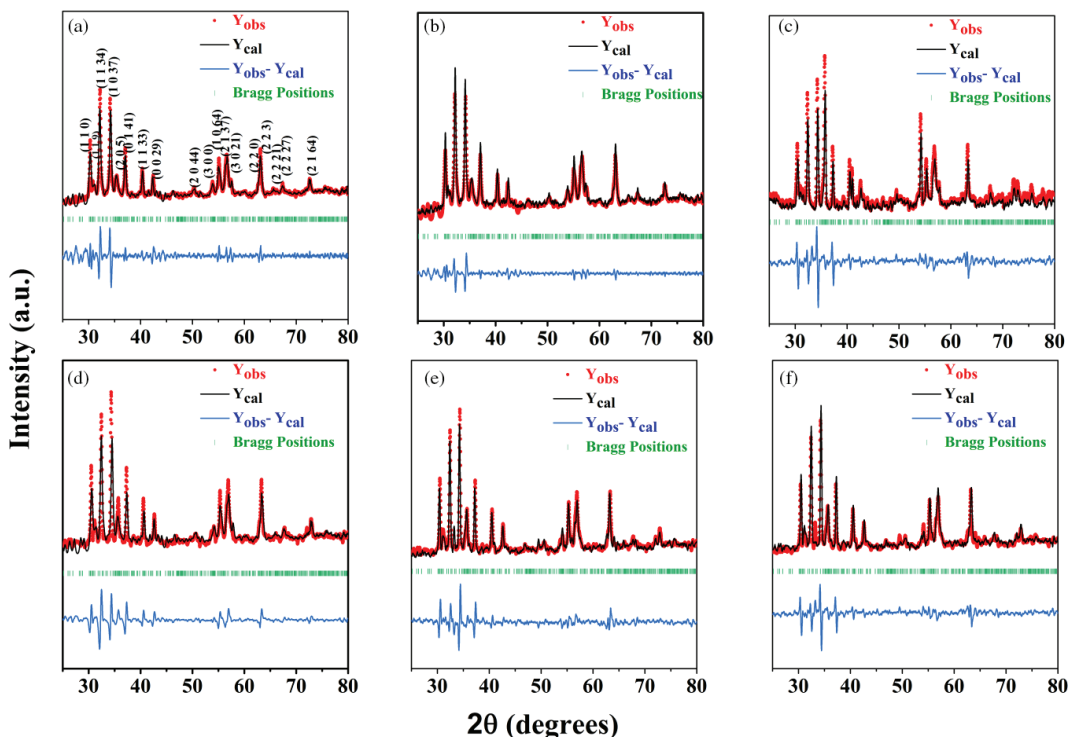
Fig. 2. The refined XRD patterns of $(Ba_{1-3x}La_{2x})_4Co_2Fe_{36}O_{60}$ solid solution for (a) $x = 0$, (b) $x = 0.05$, (c) $x = 0.10$, (d) $x = 0.15$, (e) $x = 0.20$ and (f) $x = 0.25$.

Table 1. Values of parameters obtained from the refinement of $(Ba_{1-3x}La_{2x})_4Co_2Fe_{36}O_{60}$.

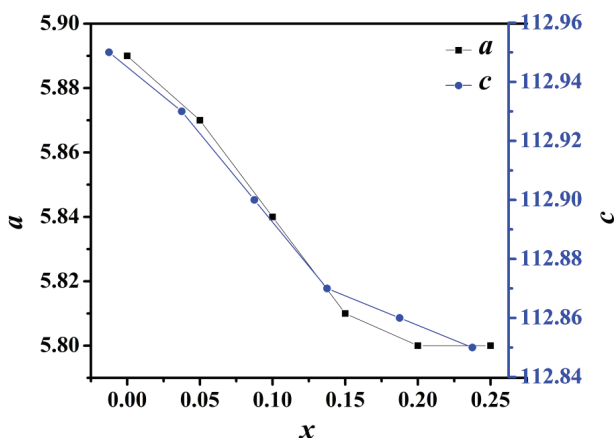| x	a (Å)	c (Å)	c/a	Volume (Å^3)	GOF
0	5.89	113.17	19.21	3926.10	1.41
0.05	5.88	112.80	19.18	3899.99	1.50
0.10	5.87	112.45	19.15	3874.67	1.72
0.15	5.86	112.21	19.14	3853.24	1.52
0.20	5.86	112.06	19.12	3848.09	2.11
0.25	5.86	112	19.11	3846.03	1.99

Fig. 3. Variations in the values of lattice parameters a and c.

that the sample with $x = 0.15$ has possessed a comparatively high magnetization value.

6. Dielectric Properties

6.1. Complex impedance analysis

The variations in the real (Z') and imaginary (Z'') parts of impedance with respect to frequency at different temperatures for the respective compositions are given in Figs. 6(a)–6(f) and 7(a)–7(f), respectively. At lower frequency, the magnitudes of both Z' and Z'' are found to decrease with increase in temperature, whereas at higher frequencies, the values of Z' merge for all the temperatures. This decrease in the value of Z' at lower frequencies may be due to the increase in the AC conductivity with temperature. The merging of Z' at higher frequencies gives hint about the possible release of space charges with consistent reduction in potential barrier.[26–29] Similarly, consolidation in Z'' at higher-frequency range suggests the reduction in space charge at grain boundaries which indicates the thermally activated relaxation response.[26,30] Moreover, the existence of immobile species at lower temperature along with the defect/vacancies at higher temperatures is responsible for the occurrence of double relaxation peaks in Z''.[31,32]

Figures 8(a)–8(f) display the Nyquist plots (Z' versus Z'') at different temperatures (250–300°C) taken over a wide frequency range (100 Hz–1 MHz). There is a clear evidence of two semicircular arcs within the selected temperature
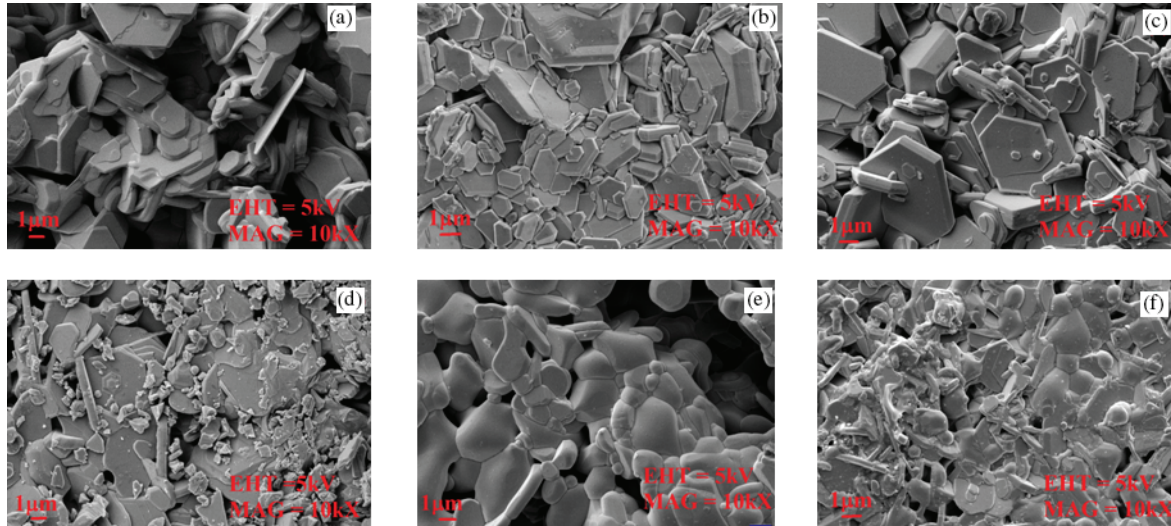
Fig. 4.   The images of surfaces of samples with (a) $x = 0$, (b) $x = 0.05$, (c) $x = 0.10$, (d) $x = 0.15$, (e) $x = 0.20$ and (f) $x = 0.25$.

Table 2.   The calculated values of grain size, standard deviation in grain size and density.

Composition (x)	Grain size (µm)	Standard deviation	Experimental density (g·cm⁻³)
0	4.50	0.0031	4.39
0.05	4.31	0.037	4.24
0.10	3.99	0.032	3.65
0.15	3.97	0.035	3.46
0.20	3.88	0.035	3.17
0.25	3.87	0.031	3.14

Table 3.   The values of saturation magnetization, coercive field and remnant magnetization for all the samples.

Composition (x)	M_s (emu/g)	M_r (emu/g)	H_c (kOe)
0	48.19	7.69	0.139
0.05	60.98	9.82	0.163
0.10	73.27	27.31	0.74
0.15	73.31	38.89	1.77
0.20	40.27	20.50	1.55
0.25	37.22	19.27	1.76

Table 4.   The comparison of magnetization values for different materials from the literature.

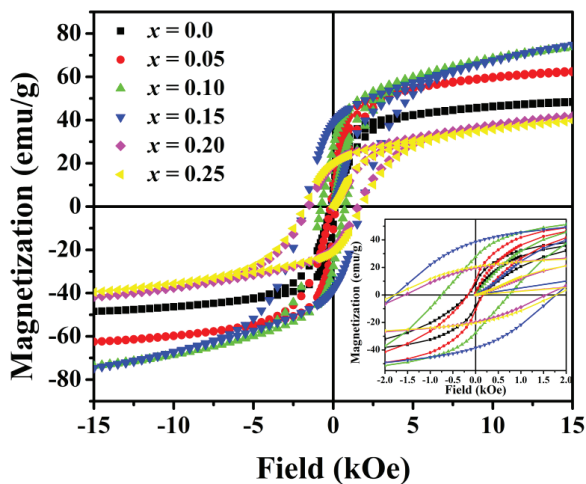| Composition	M_s (emu/g)	H_c (kOe)	Source
$Ba_4Co_2Fe_{36}O_{60}$	51.5	0.590	Ref. 2
$Ba_4Zn_2Fe_{36}O_{60}$	59	0.182	Ref. 3
$Ba_4Ni_2Fe_{36}O_{60}$	46	0.380	Ref. 12
$Ba_4Fe_2Fe_{36}O_{60}$	67	0.47	Ref. 16
$Ba_4Cu_2Fe_{36}O_{60}$	70	0.30	Ref. 16
$(Ba_{1-3x}Bi_{2x})_4Co_2Fe_{36}O_{60}$ $(x = 0.10)$	63.5	0.056	Ref. 25
$(Ba_{1-3x}Bi_{2x})_4Co_2Fe_{36}O_{60}$ $(x = 0.15)$	55.3	0.302	Ref. 25
$(Ba_{1-3x}La_{2x})_4Co_2Fe_{36}O_{60}$ $(x = 0.10)$	73.27	0.740	This work
$(Ba_{1-3x}La_{2x})_4Co_2Fe_{36}O_{60}$ $(x = 0.15)$	73.31	1.77	This work

Fig. 5.   The room-temperature magnetization versus field profiles (*M–H* loops).

range having their centers below the real axis which indicates non-Debye relaxation time.[31,33] Such behavior can be corelated with various factors including grains, grain boundary, atomic defect distribution and stress–strain phenomenon.

The semicircle at higher frequency is linked to bulk (grain) contribution and the one at lower frequency to the grain boundary contribution. The modeling of impedance data has been done by using a circuit of two resistances (*R*) and two capacitance phase elements (CPEs) in parallel as shown in the inset of Fig. 8(a). To overcome the dispersion

Fig. 6. The real part of impedance (Z') versus frequency for (a) $x = 0$, (b) $x = 0.05$, (c) $x = 0.10$, (d) $x = 0.15$, (e) $x = 0.20$ and (f) $x = 0.25$.

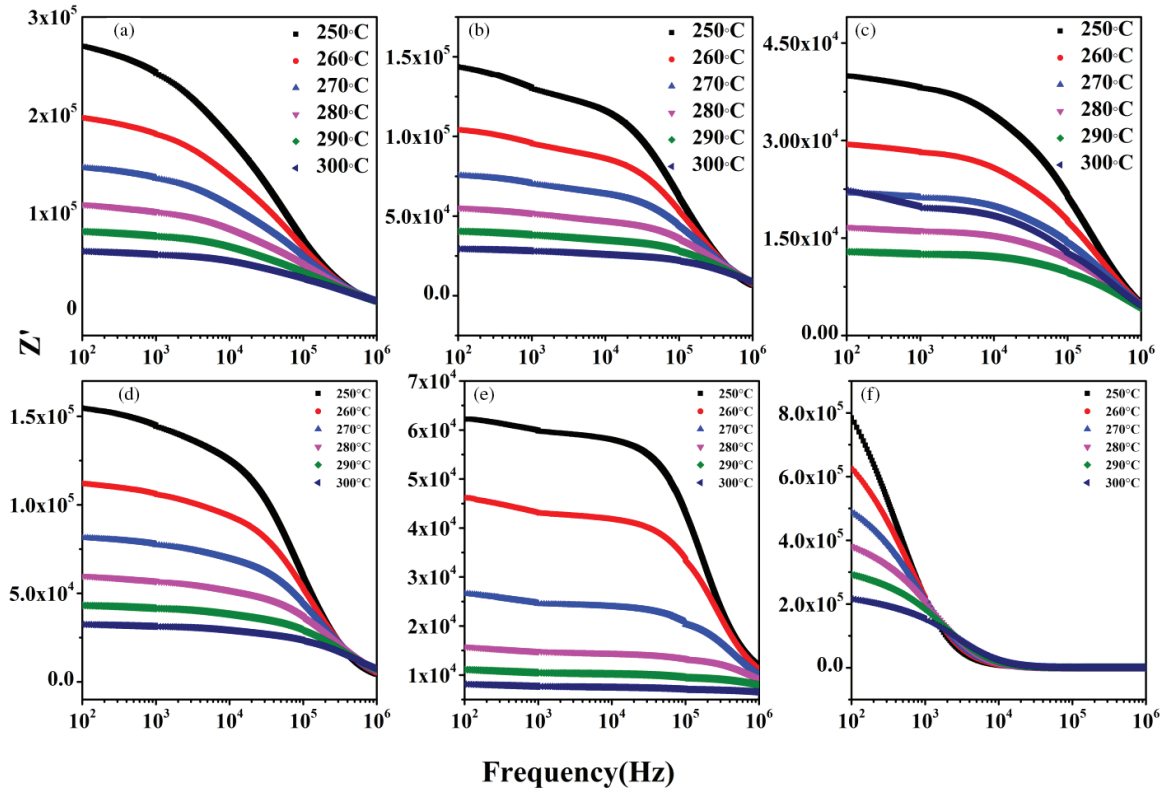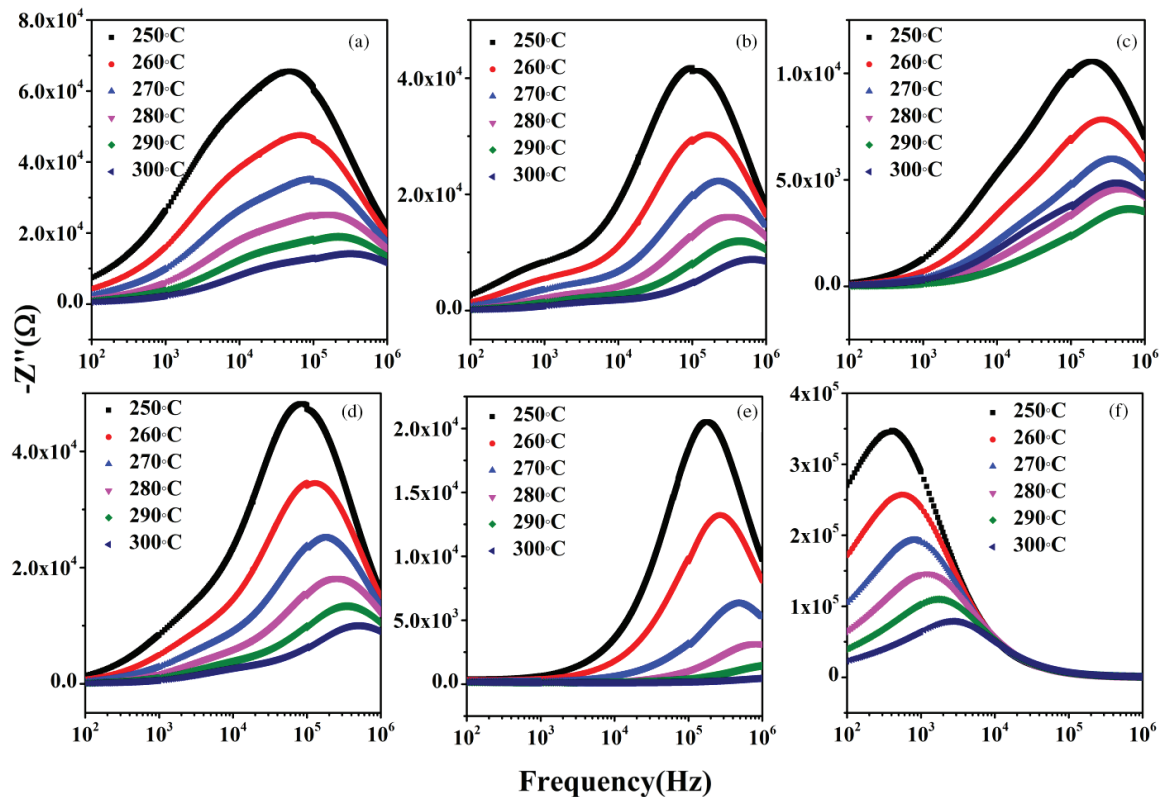Fig. 7. The imaginary part of impedance (Z'') versus frequency for (a) $x = 0$, (b) $x = 0.05$, (c) $x = 0.10$, (d) $x = 0.15$, (e) $x = 0.20$ and (f) $x = 0.25$.
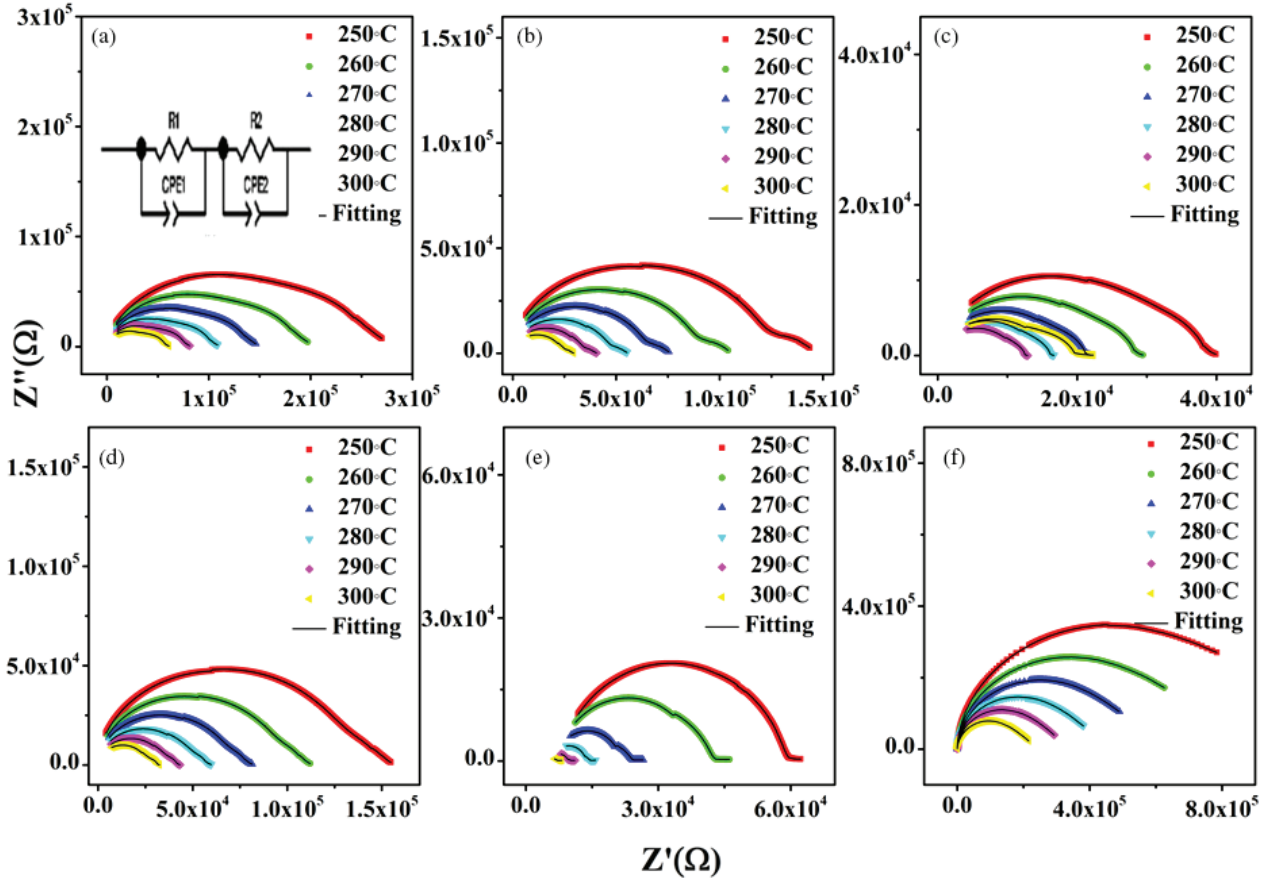
Fig. 8.　Nyquist plots (Z' versus Z'') for (a) $x = 0$, (b) $x = 0.05$, (c) $x = 0.10$, (d) $x = 0.15$, (e) $x = 0.20$ and (f) $x = 0.25$.

and nonlinearity and for more accurate fitting, CPE is used instead of capacitance to express the behaviors of grain and grain boundary regions.[34] The impedance of CPE can be calculated by: $Z_{\mathrm{CPE}} = 1/(i\omega)^{\beta}\mathrm{CPE}$, where $\beta \leq 1$. The circuit corresponding to grain consists of R_1 and CPE_1, whereas R_2 and CPE_2 correspond to the circuit of the grain boundary. The semicircles can be represented by: $Z^*(\omega) = Z' + iZ''$, where

$$Z' = \frac{R_1}{1+\left(\omega_1 R_1 C_1\right)^2} + \frac{R_2}{1+\left(\omega_2 R_2 C_2\right)^2}, \qquad (1)$$

$$Z'' = \frac{\omega_1 R_1^2 C_1}{1+\left(\omega_1 R_1 C_1\right)^2} + \frac{\omega_2 R_2^2 C_2}{1+\left(\omega_2 R_2 C_2\right)^2}, \qquad (2)$$

where (R_1, C_1, ω_1) and (R_2, C_2, ω_2) are the resistances, capacitances and peak frequencies of the grain and grain boundary semicircles, respectively. The intercept on Z'-axis provides the value of resistance, whereas the capacitances can be calculated by the formulae

$$C_1 = \frac{1}{\omega_1 R_1}, \qquad (3)$$

$$C_2 = \frac{1}{\omega_2 R_2}. \qquad (4)$$

The values of parameters obtained from the fitting of semicircles for all the samples are given in Table 5.

6.2. *Electrical modulus analysis*

Modulus analysis is a well-represented way to study the dielectric relaxation process for the materials which show a low value of capacitance. The dielectric response of non-conducting materials can be calculated by the introduction of modulus analysis. Moreover, the complex modulus provides an alternative approach to analyze the electrical response of the materials and has been adopted by scientists to study the relaxation phenomena in ceramic materials and ionic conductors. Additionally, this concept helps to confirm ambivalence due to the grain or grain boundary effect at higher temperatures which may not be established from the complex impedance plots. The complex modulus is described by

$$M^*(\omega) = M'(\omega) + iM''(\omega). \qquad (5)$$

Table 5. The values of nonlinear fitting constant obtained from the real part of dielectric constant, imaginary part of dielectric constant and electrical modulus.

| Temperature (°C)	α ($x=0$)			α ($x=0.05$)			α ($x=0.10$)			α ($x=0.15$)			α ($x=0.20$)			α ($x=0.25$)		
	ε'	ε''	M''	ε'	ε''	M''	ε'	ε''	M''	ε'	ε''	M''	ε'	ε''	M''	ε'	ε''	M''
250	0.49	0.91	0.39	0.31	0.16	0.62	0.36	0.20	0.31	0.35	0.30	0.68	0.16	0.59	0.46	0.34	0.10	0.72
260	0.50	0.11	0.35	0.29	0.18	0.60	0.35	0.50	0.25	0.34	0.60	0.66	0.16	0.97	0.44	0.34	0.09	0.73
270	0.52	0.30	0.32	0.26	0.14	0.57	0.35	0.10	0.18	0.33	0.10	0.64	0.15	0.62	0.42	0.35	0.07	0.73
280	0.53	0.34	0.29	0.25	0.16	0.55	0.35	0.17	0.08	0.31	0.26	0.61	0.14	0.18	0.39	0.37	0.06	0.74
290	0.54	0.12	0.25	0.24	0.18	0.53	0.37	0.23	0.04	0.29	0.29	0.61	0.14	0.15	0.36	0.38	0.05	0.73
300	0.56	0.29	0.16	0.24	0.16	0.53	0.40	0.31	0.04	0.27	0.72	0.60	0.14	0.20	0.31	0.40	0.08	0.71
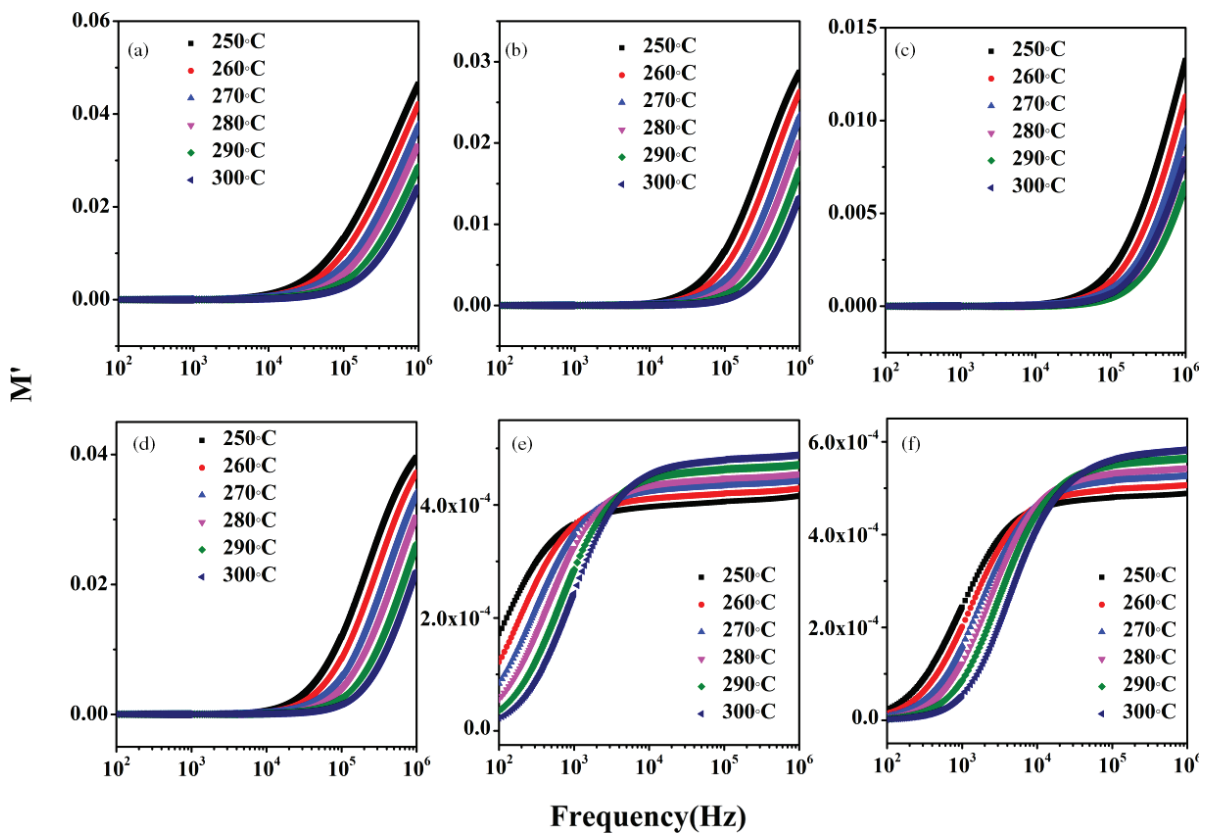
Fig. 9. The real part of electrical modulus (M') versus frequency at different temperatures for (a) $x=0$, (b) $x=0.05$, (c) $x=0.10$, (d) $x=0.15$, (e) $x=0.20$ and (f) $x=0.25$.

Frequency dependence of the real part of electrical modulus (M') at different temperatures for all the samples is given in Figs. 9(a)–9(f). It can be clearly seen from the figure that M' approaches zero in the lower-frequency region, while it exhibits continuous dispersion towards higher-frequency side with the rise in temperature.

Such behavior can be related to the absence of a restoring force controlling the mobility of charge carriers under the influence of an induced electric field.[28,35] This nature supports the short-range mobility of charge carriers for conduction phenomenon.[35]

The changes of imaginary part of the electrical modulus (M'') with respect to frequency at different temperatures are shown in Figs. 10(a)–10(f). The peak in M'' shifts towards higher frequency as the temperature increases, which gives indication about the hopping mechanism electrical conduction in all the samples. The asymmetric modulus peak-broadening behavior shows the non-Debye type of relaxation.[28,33] The positioning of the peak is indicative of the relaxation from long-range to short-range mobility with increases in frequency. The fitting of the experimental data has been done
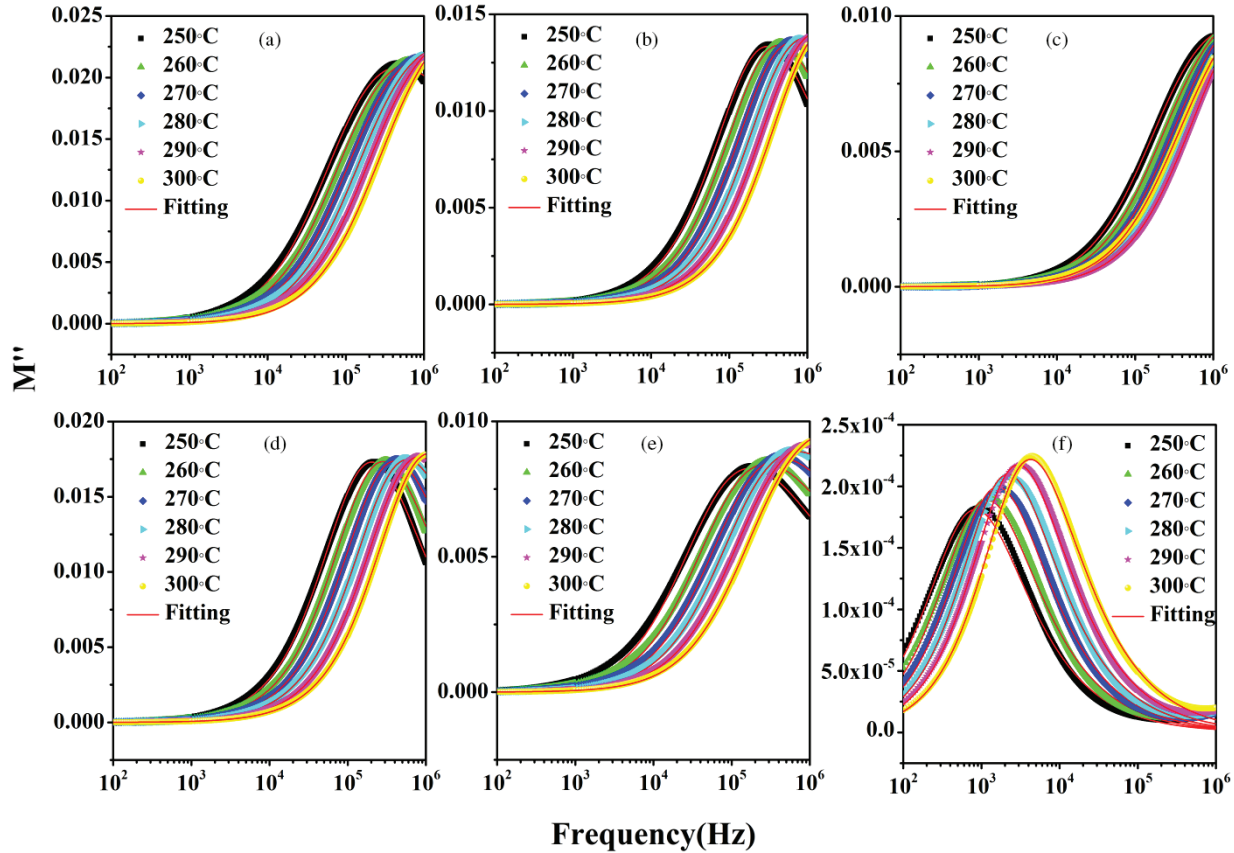
Fig. 10.   The imaginary part of electrical modulus (M'') versus frequency at different temperatures for (a) $x = 0$, (b) $x = 0.05$, (c) $x = 0.10$, (d) $x = 0.15$, (e) $x = 0.20$ and (f) $x = 0.25$.

by using the theoretical model known as the Kohlrausch–William–Watts (KWW) function (Bergman-modified KWW function), i.e., by[36,37]

$$M'' = \frac{M''_{max}}{(1-\beta)+\frac{\beta}{(1+\beta)}\left[\beta\left(\frac{\omega_{max}}{\omega}\right)+\left(\frac{\omega}{\omega_{max}}\right)^{\beta}\right]}, \quad (6)$$

where M''_{max} is the peak value of M'', ω_{max} is the frequency where the peak occurs and β is the fitting constant. Undoubtedly, Fig. 10 shows that the experimental data matches quite well with the theoretical data which has been obtained from fitting. The values of nonlinear fitting parameters are given in Table 5.

6.3.   *Dielectric dispersion*

The variations in the real (ε') and imaginary (ε'') parts of dielectric constant as a function of frequency (100 Hz–1 MHz) at different temperatures are shown in Figs. 11(a)–11(f) and 12(a)–12(f), respectively. At lower frequencies, both ε' and ε'' have large values which decrease rapidly in the low-frequency region and slowly in the higher-frequency region. Such type of behavior can be explained by the dipole

relaxation phenomenon.[38] According to this phenomenon, the net polarization of a dielectric material is the sum of several types of polarizations including dipolar, electronic, ionic and interfacial ones. All of them respond well to the induced electric field in the low-frequency region and result in a high value of total polarization and in turn attributed to high values of both ε' and ε''. However, some of the polarizations do not switch accordingly to the time-varying electric field in the high-frequency region. As a result, these orientations do not contribute to net polarization of the material and therefore resulting in low values of both ε' and ε''. In the low-frequency region, the value of dielectric constant increases with increase in temperature from 250°C to 300°C. This result shows an enhancement in the movement of charged carriers with rise in temperature. The Cole–Cole relaxation model is used to explain the relaxation phenomenon of all prepared samples.[39] According to this model,

$$\varepsilon'(\omega) = \varepsilon_{\infty} + (\varepsilon_s - \varepsilon_{\infty})\frac{\left(1+(\omega\tau)^{(1-\alpha)}\sin\alpha\pi/2\right)}{\left(1+2(\omega\tau)^{(1-\alpha)}\sin\alpha\pi/2+(\omega\tau)^{2(1-\alpha)}\right)},$$

$$(7)$$

Fig. 11.   The real part of dielectric constant (ε') versus frequency at different temperatures for (a) $x = 0$, (b) $x = 0.05$, (c) $x = 0.10$, (d) $x = 0.15$, (e) $x = 0.20$ and (f) $x = 0.25$.

$$\varepsilon''(\omega) = (\varepsilon_s - \varepsilon_\infty) \frac{\left(1 + (\omega\tau)^{(1-\alpha)} \cos\alpha\pi/2\right)}{\left(1 + 2(\omega\tau)^{(1-\alpha)} \sin\alpha\pi/2 + (\omega\tau)^{2(1-\alpha)}\right)},$$

(8)

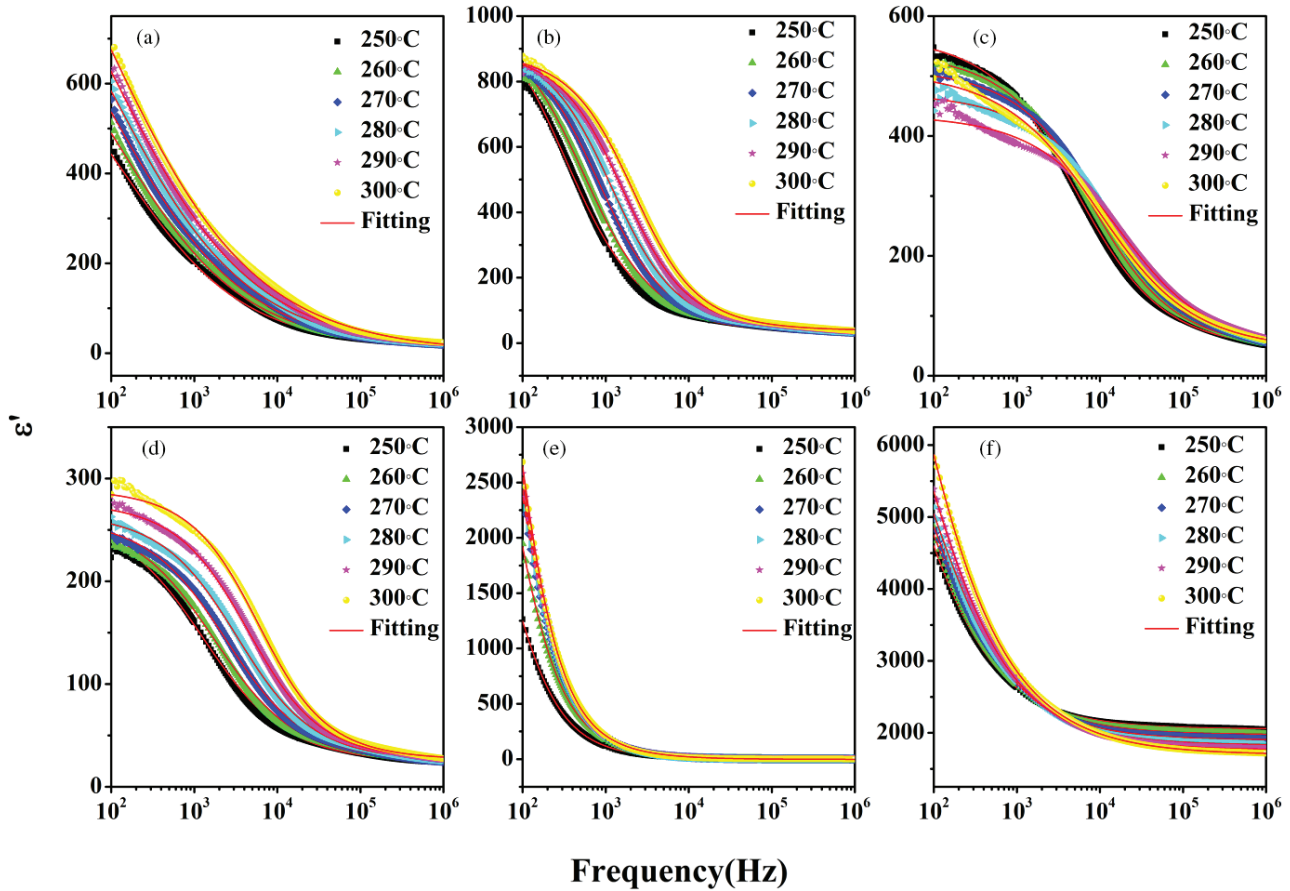where ε_∞ and ε_s are the dielectric constant values at the highest and lowest frequencies, respectively, τ is a characteristic of relaxation time of the medium and ω is the angular frequency of time-varying electric field which is 2π times the frequency. The exponent α denotes the shape parameter of spectral peaks and it varies between 0 and 1. For $\alpha = 0$, the Cole–Cole relaxation model reduces to the Debye model. The values of α obtained from the fitting are tabulated in Table 5. Clearly, the values of α are larger than 0 at all temperatures implying the relaxations are stretched. Hence, the relaxations broaden over a large range of frequency than the ideal Debye relaxation revealing the sample exhibits non-Debye relaxation.[40]

6.4.   *Electrical conductivity*

Figures 13(a)–13(f) show the variations in electrical conductivity as a function of frequency for all the samples at various temperatures. The universal law for conductivity, i.e., Jonscher's power law, has been used to analyze the frequency dependence of AC conductivity,[41]

$$\sigma_{ac} = \sigma_{dc} + A\omega^n,$$

(9)

where A represents the dispersion parameter and n is the dimensionless frequency exponent. A describes the power of polarizability and n indicates the interaction between mobile ions and the lattice around them.[42] For $n < 1$, the translational motion of charge carriers with sudden hopping dominates, whereas $n > 1$ represents the localized hopping of charge carriers without leaving the neighborhood.[43]

Figure 13 portrays two distinct regimes in the frequency-dependent conductivity plots: (i) the plateau and (ii) the dispersion region. The conductivity has been found to be frequency-independent in the plateau region (low-frequency region). On the other hand, the conductivity increases with frequency in the dispersion region (high-frequency region). In fact, the plateau region corresponds to DC conductivity (σ_{dc}), whereas the dispersion region corresponds to AC conductivity (σ_{ac}). The values of n along with DC conductivity for all the samples obtained after fitting are listed in Table 6. It is clear from the table that the value of n lies below 1 which
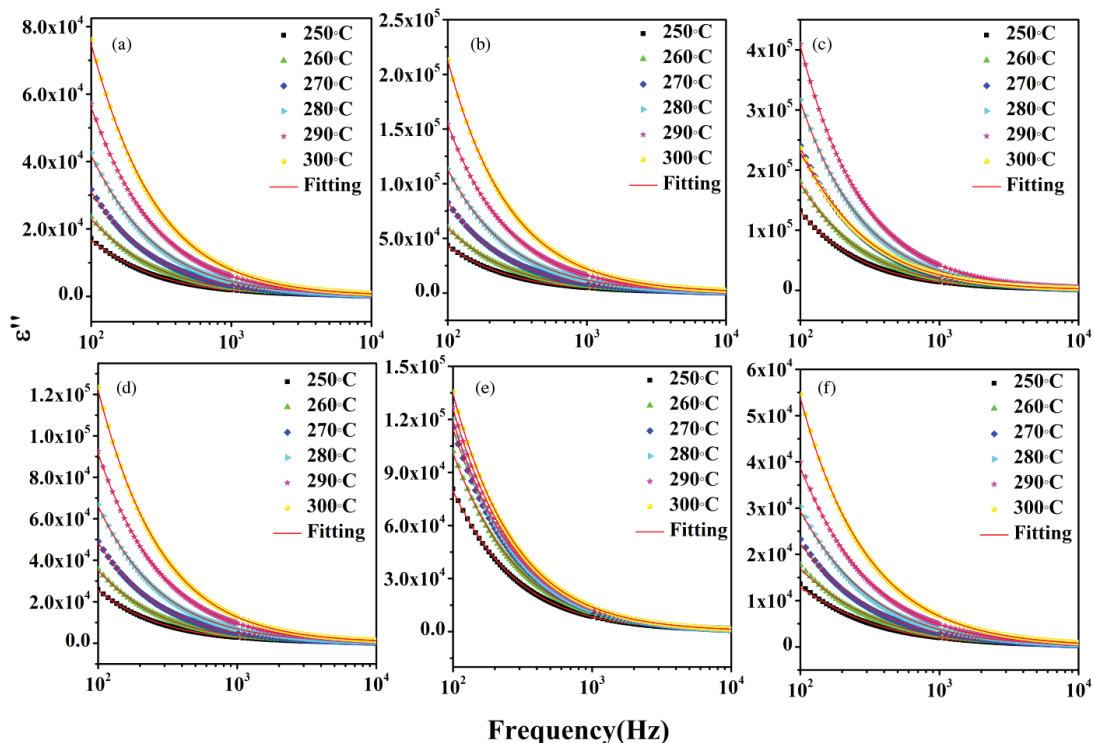
Fig. 12.   The imaginary part of dielectric constant (ε'') versus frequency at different temperatures for (a) $x = 0$, (b) $x = 0.05$, (c) $x = 0.10$, (d) $x = 0.15$, (e) $x = 0.20$ and (f) $x = 0.25$.
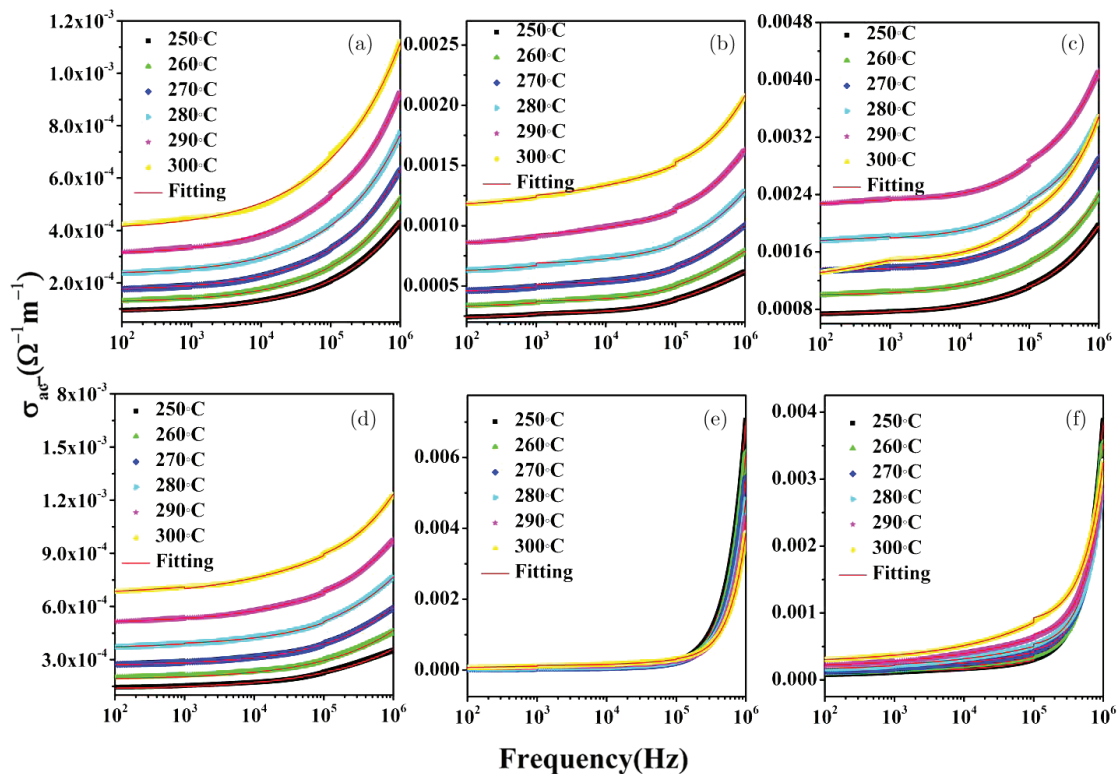

Fig. 13.   Variations in electrical conductivity as a function of frequency for (a) $x = 0$, (b) $x = 0.05$, (c) $x = 0.10$, (d) $x = 0.15$, (e) $x = 0.20$ and (f) $x = 0.25$.

Table 6.   The values of *n* along with σ_{dc} for all the samples obtained after fitting.

| Temperature (°C)	x = 0		x = 0.05		x = 0.10		x = 0.15		x = 0.20		x = 0.25	
	σ_{dc} ($\times 10^{-4}$)	n	σ_{dc} ($\times 10^{-4}$)	n	σ_{dc} ($\times 10^{-3}$)	n	σ_{dc} ($\times 10^{-4}$)	n	σ_{dc} ($\times 10^{-4}$)	n	σ_{dc} ($\times 10^{-4}$)	n
250	0.88	0.45	2.32	0.52	0.72	0.52	1.31	0.38	2.12	0.27	0.54	0.42
260	1.25	0.45	3.29	0.50	0.98	0.50	1.88	0.41	2.89	0.38	0.75	0.43
270	1.71	0.46	4.49	0.57	1.32	0.50	2.66	0.43	3.55	0.21	1.07	0.45
280	2.30	0.45	6.14	0.53	1.74	0.51	3.68	0.44	4.27	0.41	1.38	0.40
290	3.04	0.43	8.35	0.48	2.25	0.51	5.13	0.44	5.12	0.43	1.83	0.37
300	4	0.41	11.5	0.40	1.35	0.46	6.82	0.42	6.08	0.43	2.45	0.33
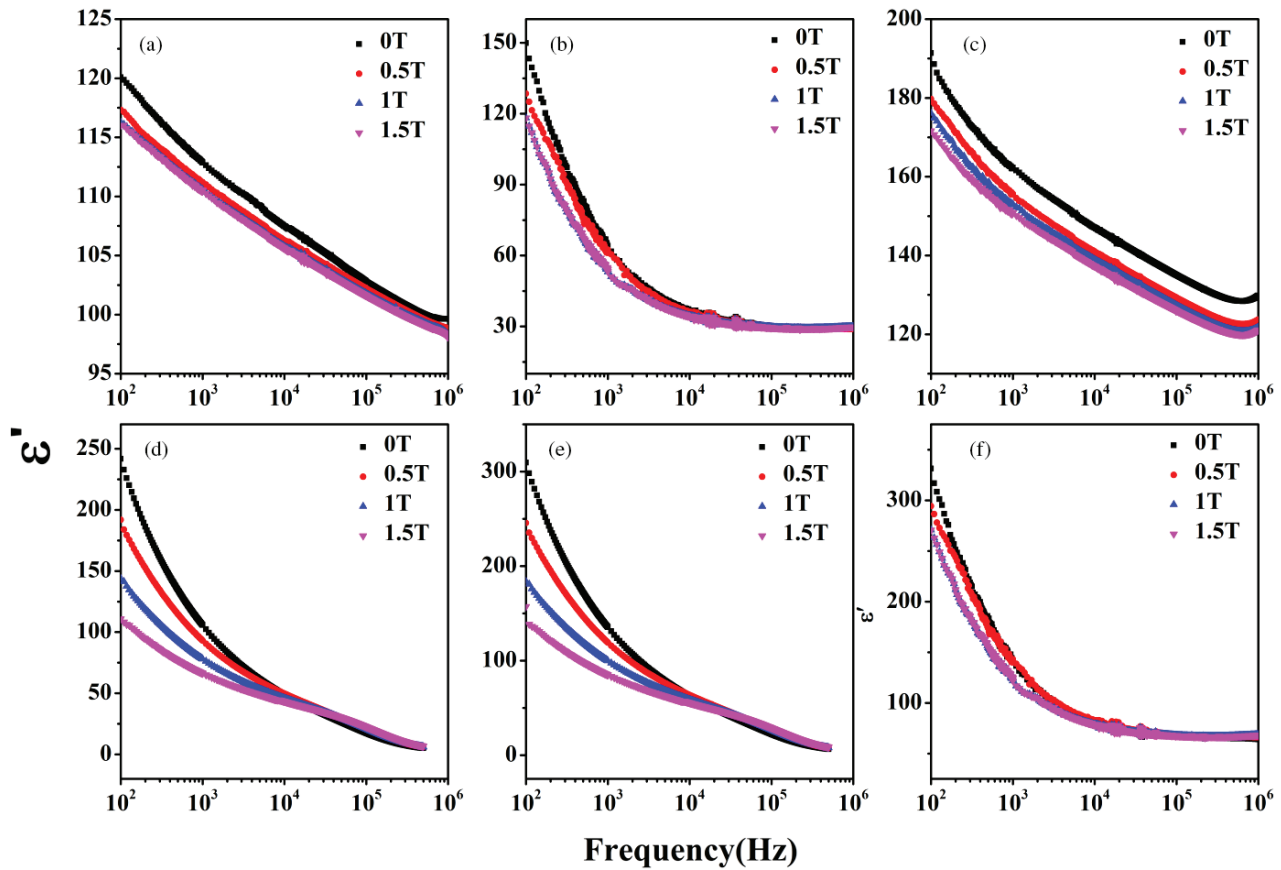
Fig. 14.   The dielectric constant (ε') versus frequency profiles for (a) x = 0, (b) x = 0.05, (c) x = 0.10, (d) x = 0.15, (e) x = 0.20 and (f) x = 0.25.

indicates the occurrence of sudden hopping phenomenon with translational motion of carriers.

6.5.   *Magneto-dielectric response*

For the investigation of magneto-dielectric response, the frequency-dependent dielectric measurements have been performed for all the samples at room temperature. The dielectric constant (ε') versus frequency profiles for all the samples at different magnetic fields (0, 0.5, 1 and 1.5 T) are given

in Figs. 14(a)–14(f). It is clear from the figure that at lower-frequency range, the value of ε' decreases with increase in magnetic field from 0 T to 1.5 T. These results inform that the dielectric constant can be easily modulated by the external magnetic field, providing significant information for the subsequent discussions of magneto-dielectric effect at some selected temperatures. This shift in magnetic field could be a reason of space charge polarization.[44] The strength of the magneto-dielectric response (MDR%) is calculated by using the formula

Table 7. The obtained MDR% values for all the samples.

Composition (x)	MDR% at 0.5 T	MDR% at 1 T	MDR% at 1.5 T
0	2.29%	3.16%	3.37%
0.05	14.25%	21.12%	21.15%
0.10	6.10%	7.99%	10.32%
0.15	20.68%	40.57%	54.18%
0.20	18.68%	38.57%	50.21%
0.25	11.1%	18.27%	18.17%

Table 8. A comparison of magneto-dielectric response obtained from different types of hexaferrites.

Composition	MDR%	Field	Source
$Sr_3Co_2Fe_{24}O_{41}$	32.2%	125 Oe	Ref. 51
$BaFe_{10.2}Sc_{1.8}O_{19}$	10%	2.5 T	Ref. 52
$SrCo_2Ti_2Fe_8O_{19}$	6%	460 Oe	Ref. 53
$Sr_3Co_2Fe_{24}O_{41}$	10%	0.15 T	Ref. 49
$(Ba_{1-3x}La_{2x})_4Co_2Fe_{36}O_{60}$ ($x = 0.15$)	54.18%	1.5 T	This work
$(Ba_{1-3x}La_{2x})_4Co_2Fe_{36}O_{60}$ ($x = 0.20$)	50.21%	1.5 T	This work

$$\text{MDR}\% = \frac{\varepsilon'(H) - \varepsilon'(0)}{\varepsilon'(0)} \times 100, \qquad (10)$$

where $\varepsilon'(H)$ and $\varepsilon'(0)$ are the values of dielectric constant at field H and without magnetic field, respectively. The values of MDR% obtained with the help of the above formula are listed in Table 7. Hence, it is evident that the sample with $x = 0.15$ has shown the maximum response among all the samples. It is worth to remind here that the sample with $x = 0.15$ has given the maximum magnetization. This behavior can be well explained by the magnetic field-induced strain phenomenon. The applied magnetic field induces magnetization and therefore leads to strain in the material. This induced strain generates stress and produces some amount of electric field in the sample, and therefore, the dielectric properties of the sample get modified.[45] Since the sample with $x = 0.15$ has shown the maximum magnetization, so it is obvious that it will show the maximum magneto-dielectric response as well. The hexaferrites belonging to multiferroic family show the magneto-dielectric behavior.[46–49] A comparison of magneto-dielectric response obtained from different types of hexaferrites is given in Table 8. Clearly, the proposed compositions of this work have shown a comparatively high value of MDR%.

7. Conclusion

The U-type hexaferrites $(Ba_{1-3x}La_{2x})_4Co_2Fe_{36}O_{60}$, where $x = 0, 0.05, 0.10, 0.15, 0.20$ and 0.25, have been prepared by auto-combustion route. All the samples have shown hexagonal structure with $R3m$ symmetry which has been confirmed by the XRD analysis. The samples for which $0 < x < 0.15$ have exhibited improved magnetic properties than at $x = 0$, whereas for those samples with $0.15 < x < 0.25$, the magnetization is in decreasing order. The dielectric properties have been investigated through impedance spectroscopy. The sample with a composition of $x = 0.15$ has exhibited maximum magnetization as well as magneto-dielectric response with a magneto-dielectric coefficient of about 54.18% at 1.5 T.

References

[1] N. Dishovski, I. Nedkov, I. Razkazov and A. Petkov, Hexaferrite contribution to microwave absorbers characteristics, *IEEE Trans. Magn.* **30**, 969 (1994), doi:10.1109/20.312461.

[2] R. C. Pullar and A. K. Bhattacharya, The synthesis and characterisation of Co_2X ($Ba_2Co_2Fe_{28}O_{46}$) and Co_2U ($Ba_4Co_2Fe_{36}O_{60}$) ferrite fibres, manufactured from a sol-gel process, *J. Mater. Sci.* **36**, 4805 (2001), doi:10.1023/A:1017947625940.

[3] D. Lisjak and M. Drofenik, Synthesis and characterization of Zn_2U ($Ba_4Zn_2Fe_{36}O_{60}$) hexaferrite powder, *J. Appl. Phys.* **93**, 8011 (2003), doi:10.1063/1.1540159.

[4] S. R. Shannigrahi, W. Q. Au, V. Suresh Kumar, L. Liu, Z. H. Yang, C. Cheng, C. K. I. Tan and R. V. Ramanujan, Synthesis and electromagnetic properties of U-type hexaferrites $Ba_4B_2Fe_{36}O_{60}$ (B: Co, Ni, Cu), *J. Magn. Magn. Mater.* **325**, 63 (2013), doi:10.1016/j.jmmm.2012.08.019.

[5] K. Kamishima, R. Tajima, K. Watanabe, K. Kakizaki, A. Fujimori, M. Sakai, K. Watanabe and H. Abe, Crystallographic and magnetic properties of Cu_2U-type hexaferrite, *J. Magn. Magn. Mater.* **375**, 54 (2015), doi:10.1016/j.jmmm.2014.09.055.

[6] R. S. Meena, S. Bhattachrya and R. Chatterjee, Complex permittivity, permeability and microwave absorbing studies of ($Co_{2-x}Mn_x$) U-type hexaferrite for X-band (8.2–12.4 GHz) frequencies, *Mater. Sci. Eng. B, Solid-State Mater. Adv. Technol.* **171**, 133 (2010), doi:10.1016/j.mseb.2010.03.086.

[7] R. S. Meena, S. Bhattachrya and R. Chatterjee, Complex permittivity, permeability and wide band microwave absorbing property of La^{3+} substituted U-type hexaferrite, *J. Magn. Magn. Mater.* **322**, 1923 (2010), doi:10.1016/j.jmmm.2010.01.008.

[8] R. S. Meena, S. Bhattachrya and R. Chatterjee, Complex permittivity, permeability and microwave absorbing properties of ($Mn_{2-x}Zn_x$) U-type hexaferrite, *J. Magn. Magn. Mater.* **322**, 2908 (2010), doi:10.1016/j.jmmm.2010.05.004.

[9] S. Kumar, R. S. Meena and R. Chatterjee, Microwave absorption studies of Cr-doped Co–U type hexaferrites over 2–18 GHz frequency range, *J. Magn. Magn. Mater.* **418**, 194 (2016), doi:10.1016/j.jmmm.2016.02.084.

[10] D. Lisjak, D. Makovec and M. Drofenik, Formation of U-type hexaferrites, *J. Mater. Res.* **19**, 2462 (2004), doi:10.1557/JMR.2004.0317.

[11] D. Lisjak, V. B. Bregar, A. Znidarsic and M. Drofenik, Microwave behaviour of ferrite composites, *J. Optoelectron. Adv. Mater.* **8**, 60 (2006).

[12] D. Lisjak and M. Drofenik, The thermal stability range and magnetic properties of U-type hexaferrites, *J. Magn. Magn. Mater.* **272–276**, E1817 (2004), doi:10.1016/j.jmmm.2003.12.879.

[13] D. Lisjak, P. McGuiness and M. Drofenik, Thermal instability of Co-substituted barium hexaferrites with U-type structure, *J. Mater. Res.* **21**, 420 (2006), doi:10.1557/jmr.2006.0048.

[14] D. Lisjak and M. Drofenik, Synthesis and characterization of Zn_2U ($Ba_4Zn_2Fe_{36}O_{60}$) hexaferrite powder, Journal of applied Physics, (2003). https://doi.org/https://doi.org/10.1063/1.1540159.

15M. C. Dimri, S. C. Kashyap and D. C. Dube, Complex permittivity and permeability of Co_2U ($Ba_4Co_2Fe_{36}O_{60}$) hexaferrite bulk and composite thick films at radio and microwave frequencies, *IEEE Trans. Magn.* **42**, 3635 (2006), doi:10.1109/TMAG.2006.882378.

16M. Chandra Dimri, H. Khanduri, H. Kooskora, I. Heinmaa, E. Joon and R. Stern, Magnetic properties and 57Fe NMR studies of U-type hexaferrites, *J. Magn. Magn. Mater.* **323**, 2210 (2011), doi:10.1016/j.jmmm.2011.03.033.

17A. J. Kerecman and T. R. AuCoin, Ferromagnetic resonance in $Ba_4Zn_2Fe_{36}O_{60}$ (ZnU) and Mn-substituted ZnU single crystals, *J. Appl. Phys.* **40**, 1416 (1969).

18J. Chen, Y. Liu, Y. Wang, Q. Yin, Q. Liu, C. Wu and H. Zhang, Magnetic and microwave properties of polycrystalline U-type hexaferrite, *J. Magn. Magn. Mater.* **496**, 165948 (2020), doi:10.1016/j.jmmm.2019.165948.

19T. Honda, Y. Hiraoka, Y. Wakabayashi and T. Kimura, Refinement of crystal structure of a magnetoelectric U-type hexaferrite $Sr_4Co_2Fe_{36}O_{60}$, *J. Phys. Soc. Jpn.* **82**, 025003 (2013).

20K. Okumura, T. Ishikura, M. Soda, T. Asaka, H. Nakamura, Y. Wakabayashi, T. Kimura, K. Okumura, T. Ishikura, M. Soda, T. Asaka, H. Nakamura and Y. Wakabayashi, Magnetism and magnetoelectricity of a U-type hexaferrite $Sr_4Co_2Fe_{36}O_{60}$, *Appl. Phys. Lett.* **98**, 212504 (2014), doi:10.1063/1.3593371.

21S. Ounnunkad, Improving magnetic properties of barium hexaferrites by La or Pr substitution, *Solid State Commun.* **138**, 472 (2006), doi:10.1016/j.ssc.2006.03.020.

22J. Jia, C. Liu, N. Ma, G. Han, W. Weng and P. Du, Exchange coupling controlled ferrite with dual magnetic resonance and broad frequency bandwidth in microwave absorption, *Sci. Technol. Adv. Mater.* **14**, 045002 (2013), doi:10.1088/1468-6996/14/4/045002.

23J. J. Xu, C. M. Yang, H. F. Zou, Y. H. Song, G. M. Gao, B. C. An and S. C. Gan, Electromagnetic and microwave absorbing properties of Co_2Z-type hexaferrites doped with La^{3+}, *J. Magn. Magn. Mater.* **321**, 3231 (2009), doi:10.1016/j.jmmm.2009.05.039.

24H. Li, H. Zou, L. Yuan, J. Xu, S. Gan, J. Meng and G. Hong, Preparation and characterization of W-type hexaferrite doped with La^{3+}, *J. Rare Earths* **25**, 590 (2007).

25S. Kumar and R. Chatterjee, Complex permittivity, permeability, magnetic and microwave absorbing properties of Bi^{3+} substituted U-type hexaferrite, *J. Magn. Magn. Mater.* **448**, 88 (2018), doi:10.1016/j.jmmm.2017.06.123.

26S. Mahajan, O. P. Thakur, D. K. Bhattacharya and K. Sreenivas, Ferroelectric relaxor behaviour and impedance spectroscopy of Bi_2O_3-doped barium zirconium titanate ceramics, *J. Phys. D, Appl. Phys.* **42**, 065413 (2009), doi:10.1088/0022-3727/42/6/065413.

27T. Takenaka, H. Nagata and Y. Hiruma, Current developments and prospective of lead-free piezoelectric ceramics, *Jpn. J. Appl. Phys.* **47**, 3787 (2008), doi:10.1143/JJAP.47.3787.

28Priyanka and A. K. Jha, Electrical characterization of zirconium substituted barium titanate using complex impedance spectroscopy, *Bull. Mater. Sci.* **36**, 135 (2013), doi:10.1007/s12034-013-0420-0.

29S. Sen and R. N. Choudhary, Impedance studies of Sr modified $BaZr_{0.05}Ti_{0.95}O_3$ ceramics, *Mater. Chem. Phys.* **87**, 256 (2003).

30A. Kaushal, S. M. Olhero, B. Singh, D. P. Fagg, I. Bdikin and J. M. F. Ferreira, Impedance analysis of $0.5Ba(Zr_{0.2}Ti_{0.8})O_3$–0.5-$(Ba_{0.7}Ca_{0.3})TiO_3$ ceramics consolidated from micro-granules, *Ceram. Int.* **40**, 10593 (2014), doi:10.1016/j.ceramint.2014.03.038.

31T. Badapanda, S. Sarangi, B. Behera and S. Anwar, Structural and impedance spectroscopy study of samarium modified barium zirconium titanate ceramic prepared by mechanochemical route, *Curr. Appl. Phys.* **14**, 1192 (2014), doi:10.1016/j.cap.2014.06.007.

32M. A. Rafiq, M. N. Rafiq and K. Venkata Saravanan, Dielectric and impedance spectroscopic studies of lead-free barium-calcium-zirconium-titanium oxide ceramics, *Ceram. Int.* **41**, 11436 (2015), doi:10.1016/j.ceramint.2015.05.107.

33T. Badapanda, L. S. Cavalcante, G. E. da Luz Jr., N. C. Batista, S. Anwar and E. Longo, Effect of yttrium doping in barium zirconium titanate ceramics: A structural, impedance, modulus spectroscopy study, *Metall. Mater. Trans. A, Phys. Metall. Mater. Sci.* **44**, 4296 (2013), doi:10.1007/s11661-013-1770-3.

34F. D. Morrison, D. J. Jung and J. F. Scott, Constant-phase-element (CPE) modeling of ferroelectric random-access memory lead zirconate-titanate (PZT) capacitors, *J. Appl. Phys.* **101**, 094112 (2007), doi:10.1063/1.2723194.

35R. Ranjan, R. Kumar, B. Behra and R. N. P. Choudhary, Structural and impedance spectroscopic studies of samarium modified lead zirconate titanate ceramics, *Physica B* **404**, 3709 (2009).

36N. Ortega, A. Kumar, P. Bhattacharya, S. B. Majumder and R. S. Katiyar, Impedance spectroscopy of multiferroic $PbZr_xTi_{1-x}O_3/CoFe_2O_4$ layered thin films, *Phys. Rev. B, Condens. Matter Mater. Phys.* **77**, 014111 (2008), doi:10.1103/PhysRevB.77.014111.

37R. Bergman, General susceptibility functions for relaxations in disordered systems, *J. Appl. Phys.* **88**, 1356 (2000).

38M. Kumar and K. L. Yadav, Study of dielectric, magnetic, ferroelectric and magnetoelectric properties in the $PbMn_xTi_{1-x}O_3$ system at room temperature, *J. Phys., Condens. Matter* **19**, 242202 (2007), doi:10.1088/0953-8984/19/24/242202.

39P. R. Mason, J. B. Hasted and L. Moore, The use of statistical theory in fitting equations to dielectric dispersion data, *Adv. Mol. Relax. Process.* **6**, 217 (1974), doi:10.1016/0001-8716(74)80003-9.

40S. Havriliak and S. Negami, A complex plane representation of dielectric and mechanical relaxation processes in some polymers, *Polymer* **8**, 161 (1967), doi:10.1016/0032-3861(67)90021-3.

41J. Pal, S. Kumar, S. Kaur, P. S. Malhi, Y. Kumar, M. Singh and A. Singh, Study of the magnetic, electrical and magneto-dielectric properties and dielectric relaxation in $0.8BiFeO_3·0.2Ba_{0.8}Sr_{0.2}TiO_3$ solid solution, *Solid State Sci.* **103**, 106193 (2020), doi:10.1016/j.solidstatesciences.2020.106193.

42D. K. Pradhan, B. Behera and P. R. Das, Studies of dielectric and electrical properties of a new type of complex tungsten bronze electroceramics, *J. Mater. Sci., Mater. Electron.* **23**, 779 (2012).

43S. Patanayak, R. N. P. Choudhary and P. R. Das, Effect of Gd-substitution on phase transition and conduction mechanism of $BiFeO_3$, *J. Mater. Sci., Mater. Electron.* **24**, 2767 (2013).

44G. Catalan, Magnetocapacitance without magnetoelectric coupling, *Appl. Phys. Lett.* **88**, 102902 (2006), doi:10.1063/1.2177543.

45V. R. Palkar, D. C. Kundaliya, S. K. Malik and S. Bhattacharya, Magnetoelectricity at room temperature in the $Bi_{0.9-x}Tb_xFeO_3$ system, *Phys. Rev. B, Condens. Matter Mater. Phys.* **69**, 212102 (2004), doi:10.1103/PhysRevB.69.212102.

46T. Kimura, Magnetoelectric hexaferrites, *Annu. Rev. Condens. Matter Phys.* **3**, 93 (2012), doi:10.1146/annurev-conmatphys-020911-125101.

47T. Kimura, G. Lawes and A. P. Ramirez, Electric polarization rotation in a hexaferrite with long-wavelength magnetic structures, *Phys. Rev. Lett.* **94**, 137201 (2005), doi:10.1103/PhysRevLett.94.137201.

48Y. Kitagawa, Y. Hiraoka, T. Honda, T. Ishikura and H. Nakamura, Low-field magnetoelectric effect at room temperature, *Nature Mater.* **9**, 797 (2010), doi:10.1038/nmat2826.

49Y. Tokunaga, Y. Kaneko, D. Okuyama, S. Ishiwata, T. Arima, S. Wakimoto and K. Kakurai, Multiferroic M-type hexaferrites with a room-temperature conical state and magnetically controllable spin helicity, *Phys. Rev. Lett.* **105**, 257201 (2010), doi:10.1103/PhysRevLett.105.257201.

[50]X. Wang *et al*., Giant magnetoresistance due to magnetoelectric currents in $Sr_3Co_2Fe_{24}O_{41}$ hexaferrites, *Appl. Phys. Lett.* **105**, 112408 (2016), doi:10.1063/1.4896326.

[51]H. Izadkhah, S. Zare, S. Somu and C. Vittoria, Effects of cobalt substitutions on the magnetoelectric coupling of M-type hexaferrite films, *Appl. Phys. Lett.* **106**, 142905 (2018), doi:10.1063/1.4916102.

[52]L. Wang, D. Wang, Q. Cao, Y. Zheng, H. Xuan, J. Gao and Y. Du, Electric control of magnetism at room temperature, *Sci. Rep*. **2**, 223 (2011).